Fig. 3, WC is the main phase due to the decarburization of WC to W_2C. XRD patterns also showed that the HVOF sprayed WC based cermet coating was able to effectively inhibit the formation of the decarburization phase due to its relatively low temperature and high flame velocity. It is likely that more carbide phases would form on the surface in accordance with the EDS analysis of the coating powder. Al-containing phases may have penetrated from the intermediate linker to the surface by diffusion.

Critical components of machine and automobile are commonly produced using lamellar graphite cast iron with perlitic structure thanks to its high thermal conductivity properties. Fig. 3 shows 100x LM images of graphite lamellae of the cast iron sample polished with standard methods and etched using 5% HNO_3+95% CH_3OH.

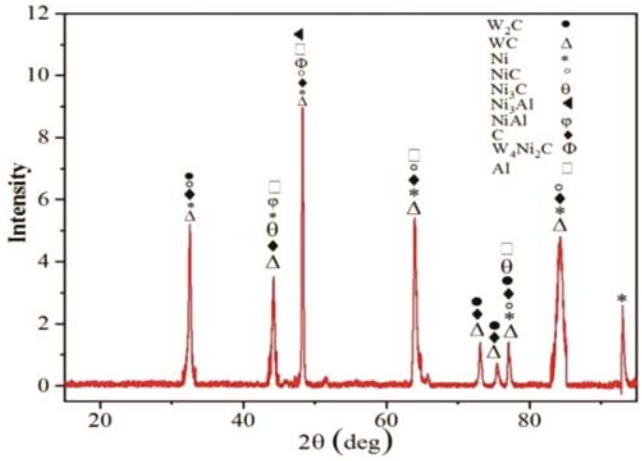

Fig. 2 — Typical XRD pattern of WC-12%Ni coating on cast iron.

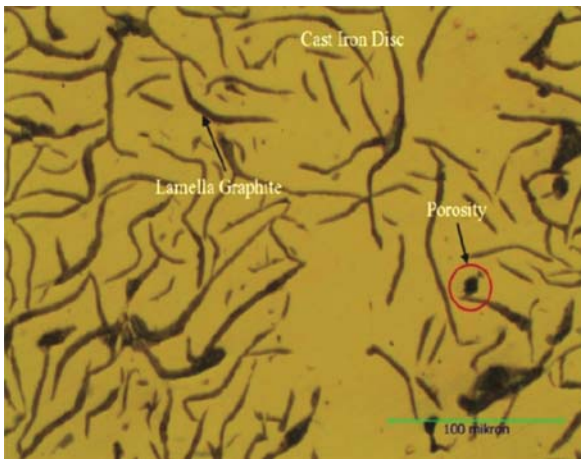

Fig. 3 — A typical LM micrograph of the GGL sample surface at 100x magnification which shows both porosity and lamella graphite.

Decked with the HVOF method using Ni5Al intermediate connector and WC-12%Ni powder, the lamellar graphite cast iron base is shown in Fig. 4 below with the LM image from cross-section at 500x magnification. The perlitic structure, in the main material, lamellar graphite and pores are observed. In the decoupled lamellar and porous structure, oxide residues are generally observed in the border areas. Tremendous mechanical interaction and a certain level of the porous structure are observed in the coating layer. Low levels of fully molten powder particles are found.

HVOF is suitable for carbide coatings depending on the atmosphere of carbide and the high speed of flames. With the HVOF technique, the powders were injected through a hot flame at a temperature of about 3500 ℃ and a speed of 1000 m/s. The powders were melted or partially melted in a 0.1-1 ms spray, as shown in Fig. 4 and Fig. 5[7, 10].

A 200x magnified SEM micrograph from the cross-section of the Ni5Al inter binding and coating layer with the HVOF method on the cast iron base material is shown in Fig. 5a. EDS analyses of the cast iron material, intermediate linker, and coating region taken from the points indicated in this micrograph are given in Fig. 5 (b, c & d). EDS Analysis of the first spot at the SEM image reflects the typical structure of the base material cast iron. Fe, Mn, Si, and C within the structure are consistent with standard values. It was determined in EDS analysis at the second spot; Al was found to be 14% in quantity atomically at Al level. The elements Fe, Mn, and C are considered to be involved in the structure through diffusion, especially due to the high heat from the base material

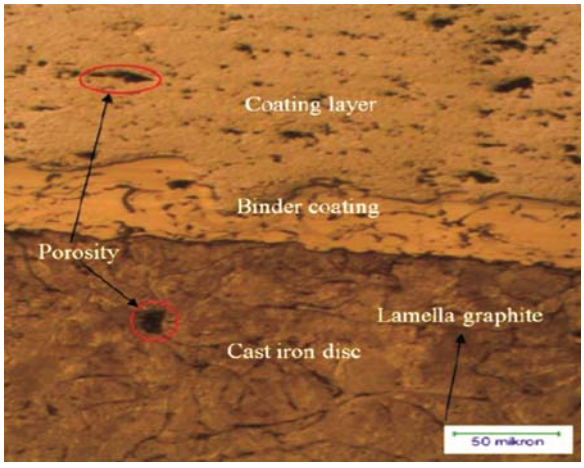

Fig. 4 — A typical LM image of the coated sample cross-section at 50x magnification which shows the coating layer, undercoat material, and cast iron substrate.

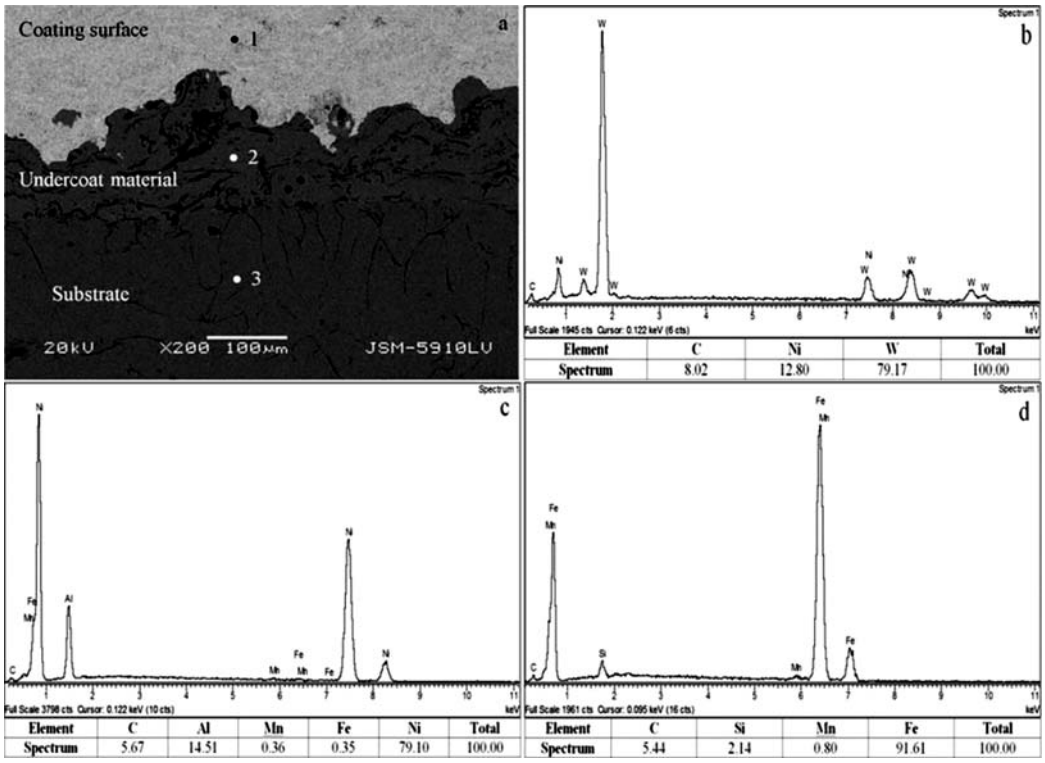

Element	C	Ni	W	Total
Spectrum	8.02	12.80	79.17	100.00

Element	C	Al	Mn	Fe	Ni	Total
Spectrum	5.67	14.51	0.36	0.35	79.10	100.00

Element	C	Si	Mn	Fe	Total
Spectrum	5.44	2.14	0.80	91.61	100.00

Fig. 5 — (a) The SEM image of WC-12%Ni coated sample x200 and (b) The corresponding EDS analyses for the 3 specific points that marked in Fig. 4 a, b, c, d.

and coating material. From EDS Analysis of the third spot, it is observed that the coating layer contains as much as 12%Ni and 8% C atomically rich in W.

When the morphology and microstructures of the magnified micrographs in 2000x and 5000x from the coating surface shown in Fig. 6 (a & b) were examined, it is possible to observe that white-colored molten and semi-molten tungsten carbides formed a good bond by settling regularly and intensively into a light gray nickel matrix. In Fig. 6 (c & d), SEM micrographs with 500x and 2000x magnification are given from the cross-section of the coating. In these micrographs, it was observed that because the Tungsten carbide particles were very small in size, they were embedded in the NiAl interlinking in the HVOF spraying method and formed a perfect bond by diffusing into the cast iron decking.

The phase of W_2C can be formed with the oxidation of WC particles in the coating powder exposed directly to the oxidizing HVOF atmosphere[39]. Bright shells surrounding WC particles (Fig. 6 (a, b & d)) were thought to represent W_2C as stated in previous studies[40]. The particle size of the powder used in the coating is small as seen in the SEM micrograph in Fig. 1. The smaller the particle size in HVOF coatings is, the greater the product temperature is. Accordingly, the level of carbide phases containing decarburization and W_2C also increases. However, the formation of new carbide phases containing W_2C has been slowed down due to the low solubility of W and C in NiAl which was used as an interconnecting agent. Therefore, it is seen to be compatible with XRD results where Ni precipitation was achieved. Additionally, the HVOF atmosphere reduces interaction between particles with the effect of high velocity, reducing carbide decomposition and oxidation. HVOF flame can cause solid preservation of carbides within the molten metal or alloy matrix. In our study, the temperature of the working flame is low and the particle size of the WC-12%Ni coating powder is small. Therefore, it was seen from micrographs that the Ni matrix fragments were dissolved and deposited, while some tungsten carbide particles remained solid. This condition is thought to form a good bond by switching smoothly with the interconnector.

It is observed from the SEM micrographs, inter-linker and main material wet each other well. This is because, in accordance with the literature[41,42], the NiAl intermetallic interlinker used in coating provides

a good mechanical grip. Additionally, during the coating process, the NiAl interbonding undergoes an exothermic reaction. This reaction gives additional high energy to the flame temperature. This concentrated high energy melts the surface and coating layer of the interconnector without causing unwanted deformation in the main material. It can also be said that the resulting energy also forms a chemical bond through micro diffusion.

The porosity was estimated by image analysis from the optical images using İmageJ software. There were about 2-3% pores in the coatings. Previous studies stated that there is a certain amount of pore in thermal spray coatings[43,44]. The NiAl bond layer was used because of its good adhesion, as well as thermal elongation between the coating and the substrate material and reduced the difference in elastic modulus. Metallurgical bond is provided in regions where the heat released as a result of exothermic reactions that oxidize nickel and aluminum; from nickel-oxide and alumina forming nickel aluminide. Furthermore, Ni-Al's being a ductile material has reduced the effect of thermal elongation and elasticity modulus differences between the coating and the cast iron base material[26].

3.2 Hardness behavior of samples

Overall hardness value in this study was measured between 200 to 1000 $HV_{0.2}$ which is associated with the various thickness of the coating layer. The hardness value of the coated sample was measured as 747 HV while the value for the uncoated sample was measured as 245 HV (Fig. 7). The hard carbide phases that make up the coating layer increased the coated sample's hardness almost three times compared to that of the cast iron sample. Since the coating hardiness is

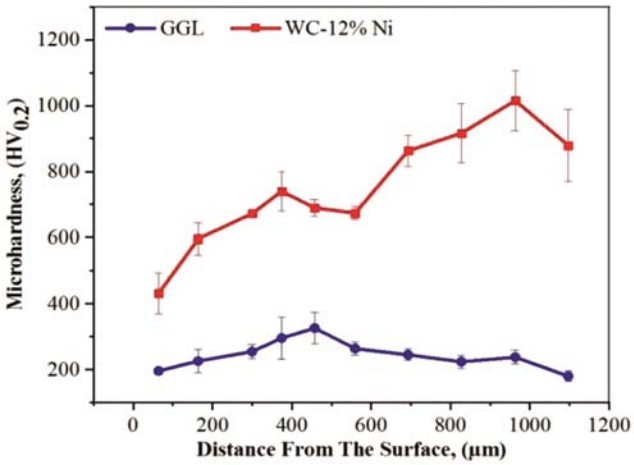

Fig. 7 — Vickers micro hardness 200g, GGL and WC-12%Ni samples.

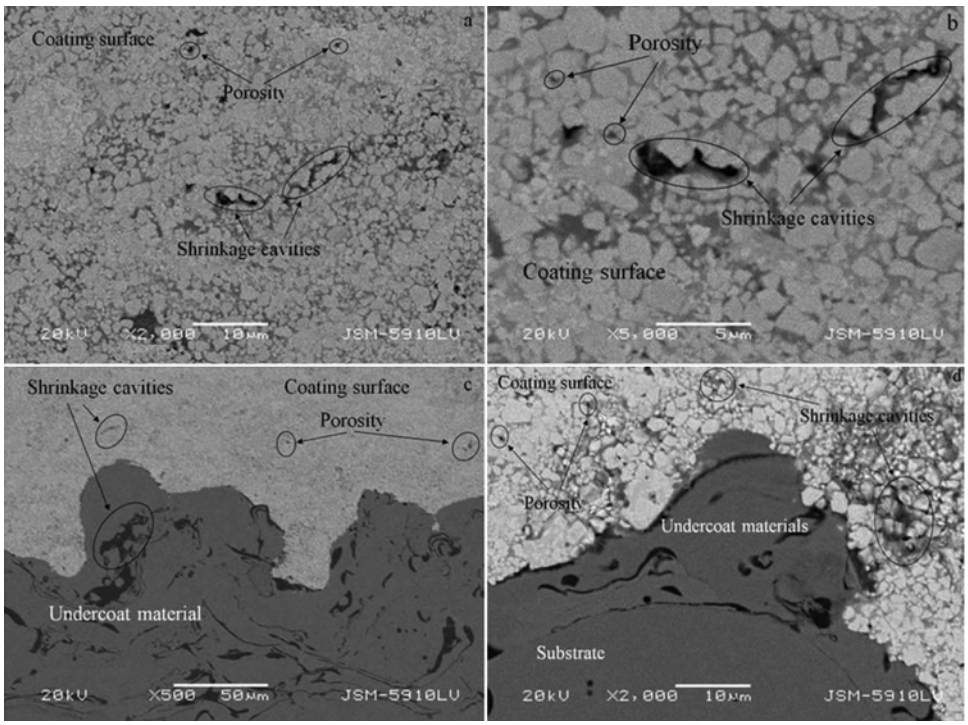

Fig. 6 — SEM images from the GGL sample coated with WC-%12Ni by HVOF spray technique at different magnifications (a) 2000x magnification at the surface, (b) 5000x magnification at the surface, (c) 500x magnification at the cross-section and (d) 2000x magnification at the cross-section; showing coating, porosity, shrinkage cavities, as well as undercoating and substrate material.

much higher than that of grey cast iron, the grey cast iron of the coated ceramic composite layer can protect against corrosion and wear. The coating hardness elevates with spray temperature, ceramic powder morphology, and coating parameters[45,46].

3.3 Wear behavior of samples

In mechanical equipment, there are different surface contact interaction processes in the elements working with two or more material groups. At this time, various wear mechanisms occur inevitably[47,48]. During this process, different combinations of wear happen simultaneously, with one wear mechanism triggering another one. These wear mechanisms are closely related to the friction properties of the material. The interaction between the frictional pairs of materials damages the surface and sub-surface layers of the material, meaning a degradation in material, shortening of service life and even economic loss[47, 48]. Thus, wear test was carried out to identify the wear mechanisms and friction properties of the samples. The amount of wear under the 10N load of the coated sample was found to be lower compared to the uncoated sample (Fig. 8), indicating the excellent bond structure of the coating with the Ni5Al Decker, and the high wear resistance of the carbide structure supported by the metal-based Ni, W, and C in the coating. Besides, due to low micro-cracks and pores on the coating layer, inevitably, the lubrication mechanism also affects.

Figure 9 (a & b) show the change in wear rates of coated and uncoated samples, depending on load and slip speed. When the load was increased from 10N to 15N, the coated sample showed higher wear resistance (Fig. 9a) since the load also increases both contact pressure and contact area. Thus, the increased contact area decreases the wear between the coating and the abrasive sphere through rapidly flattening the contact peaks, resulting in the decreased rate of wear[49-51].

Compared to the gliding rate, the coated sample showed a higher wear rate when the gliding rate increased when compared to the uncoated sample (Fig. 9b). When gliding speeds increase under certain loads, the amount of wear may decrease. Further wear of the coated specimen due to increased gliding speed suggests that it affects the tribological properties of structures such as microfractures and porosity in a negative way. It is understood from the graphic data that the amount of wear is affected by the gliding speed and the forces applied. The carbide-based coating, which has a high hardness property, showed almost the same wear rate as the uncoated sample in total.

3.4 Corrosion behavior of samples

Phase transformations, porosity, cracks, and tribological properties can significantly affect the

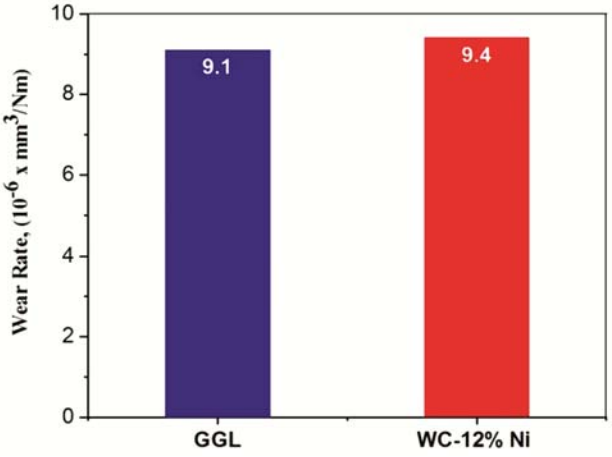

Fig.8 — The weight loss of GGL and the HVOF sprayed WC-%12Ni coatings under 10N load, suggesting a higher wear rate in the coated sample.

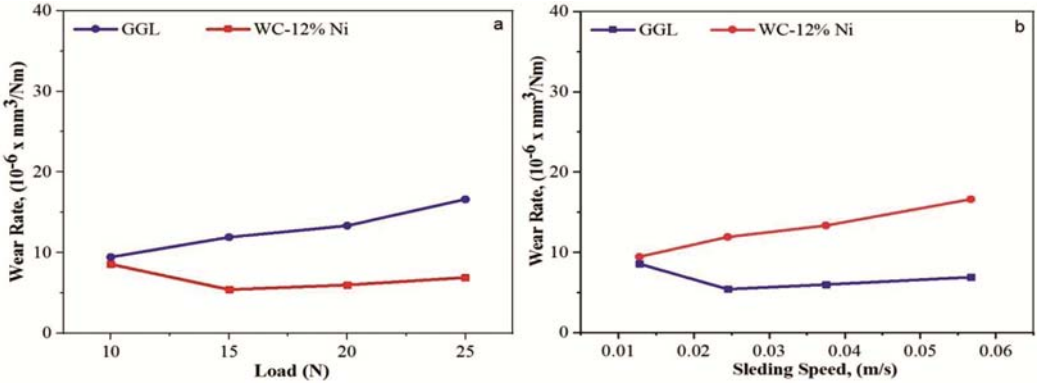

Fig. 9 — (a) The Comparisons of wear rate change in GGL and WC-%12Ni coated sample suggest lower wear rate in the coated sample depending on loads and (b) comparisons between wear rate change in GGL and WC-%12 Ni coated sample suggest lower wear rate for the coated sample associated with the sliding rate.

mechanical properties of the coating. The corrosion resistance of the coating can be decreased through pore and cracks[52-54]. Meanwhile, the increasing temperature in the coating process leads to increased amorphous-nano-crystalline phases (factor of increasing corrosion resistance) and porosity (factor of decreasing corrosion resistance), which are the two main determinants. As a result, corrosion resistance is determined by the dominant property. To achieve the desired mechanical, metallurgical and tribological properties, it is important to determine the correct process parameters, particle temperature, and specific thermal spraying requirements. The high thermal spray temperature accelerates the oxidation of the surface. Accordingly, shape-shifting phase structures occur. This may cause an undesirable amount of porosity to increase when high corrosion resistance is required[55].

Therefore, the uncoated sample reached electrolytic equilibrium in a shorter period. The E_{cor} measurement was conducted to study the chemical stability of coatings and the properties of the corrosion process, as a function of the immersion time. However, 2-3% porosity, inclusions, molten particles, carbides and micro-cracks in the sample's structure affected the formation of the open circuit potential (OCP) curve. These parameters that triggered the corrosion caused the increase of residual stresses by disrupting the homogeneous structure.

E_{corr}-t curves of the WC-%12Ni coating and cast-iron sample tested in an electrolyte solution (3.5% NaCl) are shown in Fig. 10a. The OCP value of the coating was -400 mV while the cast iron sample was measured as -675 mV. The high corrosion potential value at the start of immersion suggests that the solution has found time to reach up to the substrate as it diffuses through microfractures and pores on the surface. The potential was then gradually reduced before equilibrium potential was obtained in both samples. This behavior can be explained by the less porous structure of the Ni5Al intermediate-binding metallic coating compared to ceramic coatings. Besides, for corrosive systems, a carbide structure supported by corrosion-resistant metal-based Ni, W, and C can create a more corrosion-resistant structure than cast iron. Higher OCP dispersion and decreased over time in the coated sample indicate that the coating is more inert.

Based on the potential current density chart (Fig. 10b), the coated sample reveals that it has better corrosion resistance with more noble potentio-dynamic polarization values than the cast iron sample. The corrosion potential of the WC-%12Ni coating (-480±4 mV) is more positive compared to the cast iron sample (-680±8 mV). The coated sample and the uncoated sample revealed a similar polarization variation. Polarization behaviour is consistent with the records of OCP curves. In other words, the corrosion potential of the WC-12%Ni HVOF spray coating has shifted to more positive potential values that protect the cast iron from corrosion. Based on potentio-dynamic polarization curves, the I_{corr} value of cast iron is higher than the coating. In line with the results obtained from E_{corr} measurements, the coating exhibited a higher corrosion resistance trend compared to cast iron (Table 4). Better corrosion means lower i_{corr} and higher E_{corr}.

Table 4 — The corrosion potential and current density values of the HVOF coated and uncoated material.

Sample	(I_{cor}) I ($x10^{-6}$ A/cm^2)	(E_{cor}) (mV)
Cast Iron	8.27	-680
W_2C-%12Ni	6.2	-480

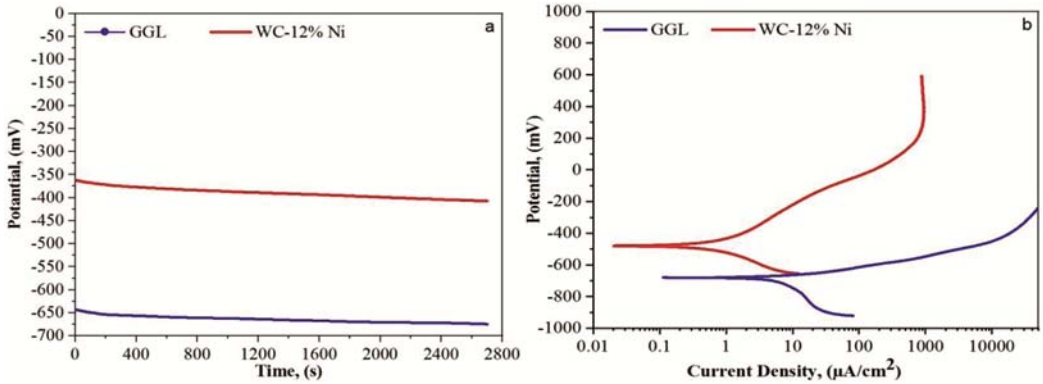

Fig. 10 — (a) OCP curves of GGL and the HVOF sprayed WC-%12Ni coated samples and (b) potentiodynamic polarization curves of GGL and the HVOF sprayed WC-%12Ni coatings in 3.5% NaCl solution.

4 Conclusions

In this study, WC-12%Ni cermet composite powder was coated with the HVOF technique on the surface of lamellar graphite cast iron. Based on the data obtained, our main results are:

(i) With the HVOF technique, WC-12%Ni cermet composite powder treatment was performed successfully on the surface of the cast iron with lamellar graphite.

(ii) The hardness of the coated surface was three times higher than that of the uncoated surface.

(iii) Coated and uncoated samples were found to have almost samedegree of wear resistance.

(iv) The coated sample showed lower i_{corr} and higher E_{corr} than the uncoated sample and tended to have higher corrosion resistance.

References

1 Shabana M M M, Sarcar K N S, Suman S & Kamaluddin S, *Mat Tod Proc*, *2* (2015) 2654.
2 Aranke O, Algenaid W, Awe S & Joshi S, *Coatings, 9(9)* (2019) 552.
3 Pantelis D I, Psyllaki P & Alexopoulos N, *Wear*, *237*(2) (2000) 197.
4 Lakhdari R, Fernandes F, Antunes P V, Mebdoua Y, Cavaleiro A & Legouera M, *Mat Res Exp*, *6*(9) (2019) 096580.
5 Lakshmi S G, Reddy G M & Roy M, *Trans Ind Inst Met*, *71*(6) (2018) 1389.
6 Wirojanupatump S, Shipway P H & McCartney D G, *Wear*, *249*(9) (2001) 829.
7 Cho T Y, Yoon J H, Hur S K, Chun H G & Zhang S H, *In Mat Sci For*, 686 (2011) 654.
8 Chun H G, Joo Y K, Yoon J H, Cho T Y, Fang W & Zhang S H, *In App Mech and Mat*, 419 (2013) 381.
9 Huang T S, *China Steel Tech Rep*, *24* (2011) 28.
10 Fang W, Cho T Y, Yoon J H, Song K O, Hur S K, Youn S J & Chun H G, *J Mat Pro Tec*, *209*(7) (2009) 3561.
11 Pogrebnyak A D, Bratushka S N, Il'yashenko M V, Makhmudov N A, Kolisnichenko O V, Tyurin Y N & Kaverin M V, *J fric wear*, *32*(2) (2011) 84.
12 Guo C, Chen J, Zhou J, Zhao J, Wang L, Yu Y & Zhou H, *Surf Coat Tech, 206* (8-9) (2012) 2064.
13 Espallargas N, Berget J, Guilemany J M, Benedetti A V & Suegama P H, *Surf Coat Tech*, *202*(8) (2008) 1405.
14 Berger L M, Saaro S, Naumann T, Wiener M, Weihnacht V, Thiele S & Suchánek J, *Surf Coat Tech*, *202*(18) (2008) 4417.
15 Mahmud T B, Farrokhzad M A & Khan T I, *Trib Online*, *12*(1) (2017) 18.
16 Sobolev V V, Guilemany J M, Miguel J R & Calero J A, *82*(1-2) (1996) 121.
17 Souza R C, Voorwald H J C & Cioffi M O H, *Surf Coat Tech*, *203*(3-4) (2008) 191.
18 Yao S H, *In Adv Mats Res,* 904 (2014) 155.
19 Bolelli G, Berger L M, Bonetti M & Lusvarghi L, *Wear*, *309*(1-2) (2014) 96.
20 Ishikawa Y, Kuroda S, Kawakita J, Sakamoto Y & Takaya M, *Surf Coat Tech*, *201*(8) (2007) 4718.
21 Junior G S, Voorwald H J C, Vieira L F S, Cioffi M O H & Bonora R G, *Pro Eng*, *2*(1) (2010) 649.
22 Güney B, Mutlu İ & Küçüksarıyıldız H, *J Poli*, *23*(3) (2020) 755.
23 Yao S H, Su Y L, Shu H Y, You Z L & Lai Y C, *In Key Eng Mat*, 739 (2017) 120.
24 Nahvi S M & Jafari M, S*urf Coat Tech*, *286* (2016) 95.
25 Sidhu V P S, Goyal K & Goyal R, *Australian J Mech Eng*, *17*(2) (2019) 127.
26 Öz A, Samur R, Mindivan H, Demir A, Sagiroglu S & Yakut A K, *Metalurgija*, *52*(3) (2013) 368.
27 Güney B & Mutlu I, *Surf Rev Lett*, *26*(10) (2019) 1950075.
28 Güney B & Mutlu İ, *Mat Testing*, *59*(5) (2017) 497.
29 Guney B, Mutlu I & Gayretli A, *J Balkan Tribo Assoc*, *22*(1 A) (2016) 887.
30 Güney B,& Mutlu I, *Mat Res Exp*, *6*(9) (2019) 096577.
31 Mutlu İ, Güney B & Erkurt İ, *Int J Auto Eng Tech*, *9*(1) (2020) 29.
32 Gtv, Gtv Spray Powder Catalogue. 2019.
33 Maranho O, Rodrigues D, Boccalini Jr M & Sinatora A, *Surf Coat Tech, 202*(15) (2008) 3494.
34 Kiilakoski J & Trache R, *J Ther Spray Tech, 28*(8) (2019) 1933.
35 Vicenzi J, Villanova D L, Lima M D, Takimi A S, Marques C M & Bergmann C P, *Mater Des*, *27*(3) (2006) 236.
36 Wen Z, Zhao Y, Hou H, Tian J & Han P, *Super Micros*, *103* (2017) 9.
37 Qiu L, Yang F, Zhang W, Zhao X & Xiao P, *Cor Sci*, *89* (2014) 13.
38 MooreD, *Ad Mat Proc*, *155*(4) (1999) 31.
39 Mateen A, Saha G C, Khan T I & Khalid F A, *Surf Coat Tech, 206*(6) (2011) 1077.
40 Zhao L, Maurer M, Fischer F, Dicks R & Lugscheider E, *Wear*, *257*(1-2) (2004) 41.
41 Pilous V & Musil J, *Wel Int*, *2*(10) (1988) 934.
42 Öz A, Gürbüz H, Yakut A K & Sağiroğlu S, *J Mech Sci Tech*, *31*(2) (2017) 535.
43 Miguel J M, Guilemany J M & Vizcaino S, *Trib Int*, *36*(3) (2003) 181.
44 Carrasquero E J, Lesage J, Puchi-Cabrera E S & Staia M H, *Surf Coat Tech*, *202*(18) (2008) 4544.
45 Shaw L L, Goberman D, Ren R, Gell M, Jiang S, Wang Y & Strutt P R, *Surf Coat Tech*, *130*(1) (2000) 1.
46 Babagiray M, Bayrakçeken H, Çakmakkaya M, Aysal F. E & Karanfil S, *Int J Aut Sci Tech*, *3*(3) (2019) 57.
47 Zou Z, Wang Y, Zhou F, Wang L, Liu S & Wang Y, *App Sur Sci*, *431* (2018) 75.
48 Tyagi R, Xiong D S, Li J & Dai J, *Wear*, *269*(11-12) (2010) 884,
49 Zhao N, Zhao Y, Wei Y, Wang X, Li J, Xu Y & Lu Z, *Tribol Int*, *135* (2019) 181.
50 Wang L, Liu S, Gou J, Zhang Q, Zhou F, Wang Y & Chu R, *App Sur Sci*, *492* (2019) 272.
51 Agunsoye J O, Ochulor E F, Talabi S I & Olatunji S, *Trib Int*, (4) (2012) 234.
52 Behazin M, Biesinger M C, Noël J J & Wren J C, *Cor Sci*, *63* (2012) 40.
53 de Villiers Lovelock H L, *J Ther Spray Tech, 7*(3) (1998) 357.
54 Wu Y, Wang B, Hong S, Zhang J, Qin Y & Li G, *Trans Ind Inst Met*, *68*(4) (2015) 581.
55 Azizpour M J & Tolouei-Rad M, *Cer Int*, *45*(11) (2019) 13934.